Chapter 6

6. REDUCED GRAPHENE OXIDE SUPPORTED Cu-DOPED ZnO NANOCATALYSTS FOR PHOTOCATALYTIC DEGRADATION OF METHYLENE BLUE

This chapter of the thesis demonstrates the complete characterization and application of reduced graphene oxide supported Cu-doped ZnO nanocatalysts. The synthesized catalyst is employed for the photocatalytic degradation of methylene blue (MB) dye. Figure 6.1 represents the molecular structure of methylene blue.

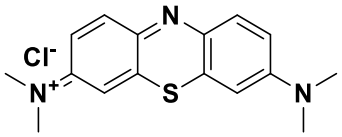

Figure 6.1 Molecular structure of methylene blue.

6.1 Prologue

Organic dyes discharged into water bodies from various industries such as textile, paper, paint, food, pharmaceuticals, and cosmetics have led to serious contamination of the environment around the globe [1, 2]. One of the most widely used aromatic dyes in industries is methylene blue (MB) [3]. MB is a heterocyclic aromatic dye pollutant of the thiazine class of dyes that degrades water quality even at trace levels [4]. Its intrinsic cytotoxicity and necrotic effects pose a serious threat to human health upon exposure [5]. Moreover, dyes in water bodies reduce sunlight penetration and hence impair the growth of aquatic plants and algae by hindering photosynthesis [6]. Therefore, it is of utmost importance to develop an efficient technique for the remediation of wastewater contaminated with these dye pollutants.

Various strategies such as adsorption [7], coagulation [8], membrane filtration [9], photocatalytic degradation [10], catalytic reduction [11], and chemical oxidation [12] for the degradation of dyes have been explored so far. Amongst these techniques, adsorption is the customarily preferred method for dye removal owing to its low cost and ease of operation as mentioned earlier in Chapter 5. However, this technique is associated with certain drawbacks such as inadequate removal of pollutants, additional treatment for adsorbent regeneration, low adsorption capacity, and poor mechanical stability of adsorbents [13, 14]. In this context, photocatalytic degradation of organic dye pollutants has garnered extensive attention owing to its high efficiency, complete

decomposition into harmless end products, facile reusability, eco-friendly, and cost-effective nature [3, 15–18].

In recent years, nanosized semiconductor metal oxides are extensively employed as photocatalysts owing to their high photosensitivity, low cost and toxicity, and eco-friendliness [19, 20]. Among various metal oxide semiconductors, ZnO has been widely studied as a photocatalytic material because of its ultraviolet (UV) light sensitivity, non-toxicity, low cost, chemical stability, biocompatibility, and excellent optoelectronic properties [21, 22]. However, due to its large band gap (3.37 eV), ZnO can be photoexcited in the UV region only. Therefore, the photocatalytic efficiency of ZnO is reduced under sunlight since the UV component of solar radiation comprises merely 4-5% of the solar spectrum [19]. To tackle this drawback of ZnO, efforts have been made to modify its band structure for achieving visible light response by doping with metals and non-metals. Among various dopants, copper ion (0.073 nm) being abundant and comparable in size to zinc ion (0.074 nm) is a promising dopant for narrowing the band gap [23–25]. Therefore, Cu-doped ZnO as a photocatalytic material has been widely investigated for enhancing photocatalytic efficiency [25, 26].

The high electron-hole recombination rate in ZnO is another limitation that deteriorates its photodegradation efficiency [27]. One common approach to address this issue involves the application of carbon-based materials which could improve charge transfer at the metal oxide-carbonic material interface [28]. In this regard, carbon nanotubes, graphite, graphitic carbon nitride, graphene oxide (GO), and reduced GO (rGO) have been found to integrate with ZnO thereby improving its photocatalytic efficiency [29–31]. Several studies reported the enhancement in photocatalytic activity of ZnO either through its doping or by adding carbon-based materials [32–35]. In this chapter, Cu-doped ZnO supported on rGO is synthesized, characterized, and employed as a catalyst for the photocatalytic degradation of MB. A comparative study of the photodegradation of MB over Cu-doped ZnO/rGO is also performed with ZnO and ZnO/rGO. The synthetic procedures for the catalysts and their characterization techniques are described in Chapter 2.

6.2 Results and discussion

6.2.1 Characterization

The powder XRD analyses of GO, pure ZnO, ZnO/rGO and Cu-doped ZnO/rGO are carried out to investigate their structural properties. It can be observed from Figure 6.1a that all the patterns for ZnO, ZnO/rGO and Cu-doped ZnO/rGO are almost identical. The diffractograms show a hexagonal wurtzite structure without the presence of other impurities. The diffraction peaks at 2θ = 31.8, 34.3, 36.1, 47.6, 56.6, 62.8, 68, and 69.1° corresponds to (100), (002), (101), (102), (110), (103), (200), and (112) planes of hexagonal wurtzite structure of crystalline ZnO (JCPDS Card No. 00-036-1415). The sharp and intense peaks of the samples are indicative of their high crystallinity. Additional peaks from copper and/or its complex oxides are not detected in the XRD pattern of Cu-doped ZnO/rGO within the detection limits. This implies that copper doping and rGO do not change the original structure of ZnO in Cu-doped ZnO/rGO sample. It should be also noted that the peaks of GO disappear in ZnO/rGO and Cu doped-ZnO/rGO which implies that GO has been completely reduced during the hydrothermal treatment of synthesis. The XRD peak of Cu-doped ZnO/rGO sample also shifts slightly towards higher Bragg's angle which is indicative of an increase in the lattice constant (Figure 6.1b). This slight change in the lattice parameter suggests the substitution of Cu ion into the Zn site [36].

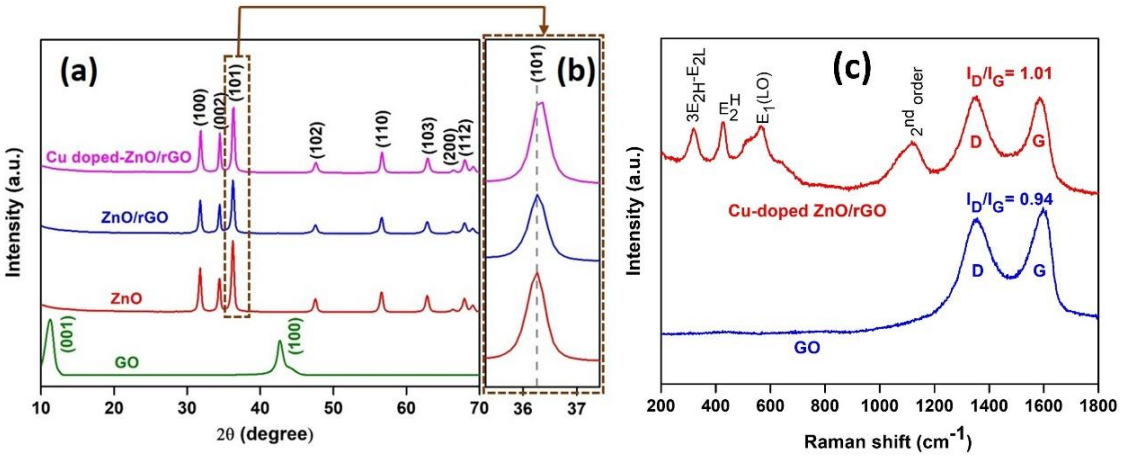

Figure 6.1 XRD pattern of synthesized samples (a), magnified view of (101) diffraction peaks of ZnO, ZnO/rGO and Cu-doped ZnO/rGO (b) and Raman spectra of GO and Cu-doped ZnO/rGO.

Figure 6.1b displays the Raman spectra of GO and Cu-doped ZnO/rGO samples. The Cu-doped ZnO/rGO sample shows a band at ~438 cm^{-1} corresponding to E_{2H} mode, which is characteristic of wurtzite ZnO [37]. The bands at 330 and 578 cm^{-1} are ascribable to $3E_{2H}$-E_{2L} and E_1(LO) phonon modes, respectively of ZnO. The broad band located at ~1147 cm^{-1} corresponds to multiple-phonon scattering processes [38]. In both the samples, the two prominent bands at 1355 cm^{-1} and 1592 cm^{-1} correspond to D and G bands, respectively. The G band is indicative of the presence of sp^2 C atoms and the D band corresponds to C–C vibrations that become active due to disorder in the graphene structure [39]. The high I_D/I_G ratio for Cu doped-ZnO/rGO (1.01) compared to that of GO (0.94) is attributable to the reduction in the average size of sp^2 domains confirming that GO has been reduced to rGO [40].

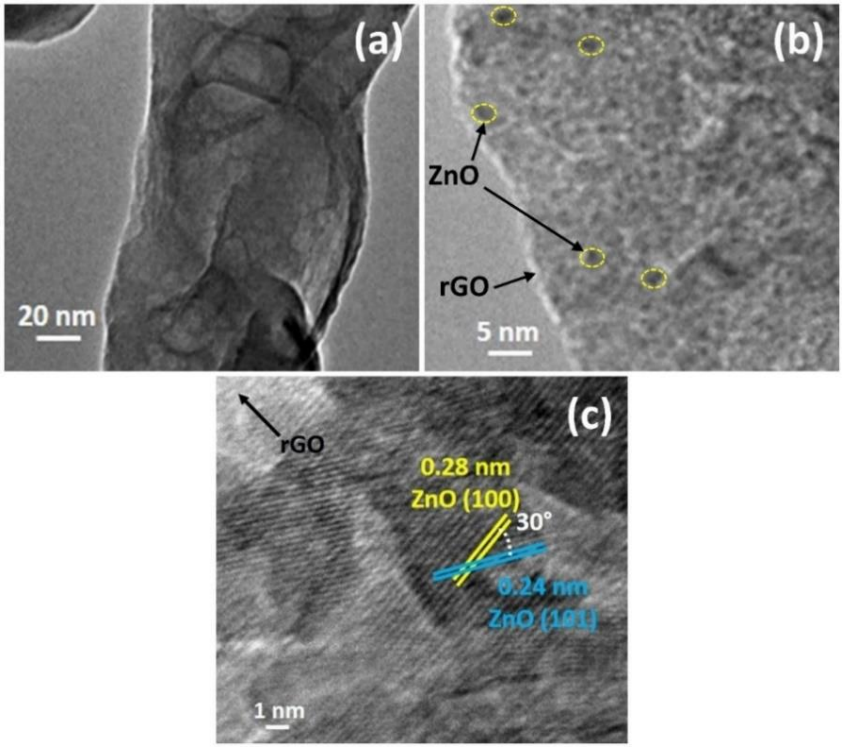

Figure 6.2 TEM micrographs at different resolution (a, b) and HR-TEM micrograph (c) of as-synthesized Cu-doped ZnO/rGO sample.

The morphology and crystallinity of the Cu-doped ZnO/rGO sample are further determined by combined TEM and HR-TEM imaging. The TEM images (Figure 6.2a and b) show that the sample is composed of rGO sheets with embedded ZnO nanoparticles on them. The oxygen-containing groups of GO sheets act as nucleation sites for the formation of ZnO nanoparticles. In Figure 6.2c, the clearly visible lattice

fringes indicate the high crystallinity of the synthesized material. The interplanar distances of 0.28 nm and 0.24 nm correspond to (100) and (101) planes of wurtzite ZnO.

The chemical composition of the Cu-doped ZnO/rGO sample is evaluated by XPS analysis as shown in Figure 6.3. The existence of three dominative elements C, O and Zn is observed in the survey spectrum (Figure 6.3a). Finding Cu in the sample is not as easy as for other elements due to the lower content of Cu as a dopant.

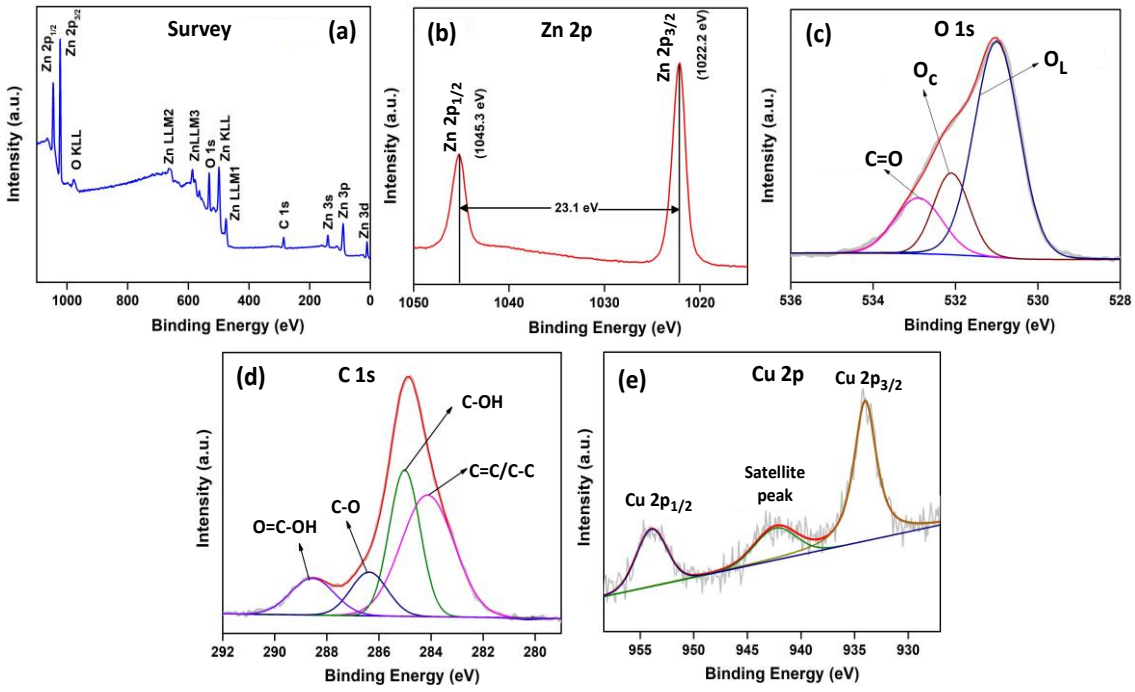

Figure 6.3 XPS survey (a), Zn 2p (b), O 1s (c), C 1s (d) and Cu 2p (e) spectra of Cu-doped ZnO/rGO.

The high-resolution Zn 2p spectrum in Figure 6.3b shows the presence of typical Zn $2p_{1/2}$ and Zn $2p_{3/2}$ peaks at 1045.3 and 1022.2 eV, respectively. The Zn 2p peaks shifted to higher positions compared to pure ZnO as reported in the literature [41]. This shift in peak is ascribable to the existence of band edge bending and hence provides evidence for Cu doping [42]. The O1s spectrum in Figure 6.3c is deconvoluted into three Gaussian peaks centered at 532.9, 532.1, and 531.0 eV. The peaks at 532.1 and 531.0 eV can be ascribed to chemisorbed oxygen and lattice oxygen in wurtzite ZnO, respectively [43]. The band at 532.9 eV corresponds to C=O bond in the Cu-doped ZnO/rGO sample. The C 1s spectrum as shown in Figure 6.3d is deconvoluted into four peaks at 288.3, 286.3, 285.2, and 284.1 eV which corresponds to O=C–OH, C–O, C–OH, and C=C/C–C functional groups of rGO, respectively [44, 45]. Although Cu peaks were absent in the

survey spectrum, the high-resolution Cu 2p spectrum in Figure 6.3e displays the presence of two peaks at 933.09 and 953.94 eV attributable to the core levels of Cu $2p_{3/2}$ and Cu $2p_{1/2}$, respectively. The appearance of a satellite peak at ~943 eV in the Cu 2p spectrum provides evidence for the presence of Cu^{2+} ions and implies its substitution at Zn^{2+} site into the ZnO lattice [46].

The band gap variation in Cu-doped ZnO/rGO as a result of Cu doping is studied by UV–vis absorption spectroscopy. The absorption spectra for ZnO, ZnO/rGO and Cu doped-ZnO/rGO are compared in Figure 6.4a. The rGO supported samples absorb substantially more towards the visible region than pure ZnO probably due to absorption by rGO sheets in these samples [47]. A strong absorption is observed in the UV region for all the samples which is generally due to the electronic transition from valence band to conduction band (O 2p→Zn 3d) characteristic of band-gap absorption of ZnO [48].

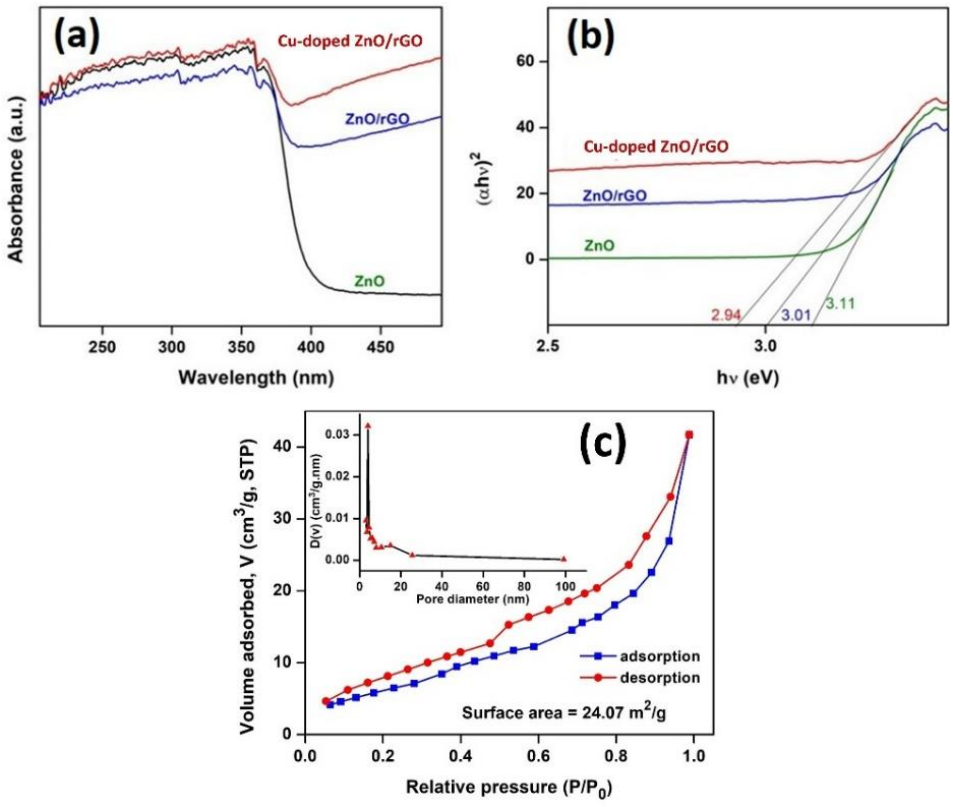

Figure 6.4 UV-vis diffuse reflectance spectra (a) and corresponding band gap energy (b) of ZnO, rGO and Cu-doped ZnO/rGO; BET isotherm of the synthesized Cu-doped ZnO/rGO sample (c); inset c: pore size distribution curve of the sample.

For direct band gap semiconductors, the band gap energy (E_g) is calculated using Tauc's equation $(\alpha h\nu)^2 = A(h\nu - E_g)$, where α is the absorption coefficient, $h\nu$ is the energy of photon and A is the proportionality constant. The band gap energy is calculated by

extrapolation of the curve to X-axis from $(\alpha h\nu)^2$ versus hν plots. Figure 6.4b displays the Tauc plots of all the samples with band gap values of 3.11, 3.01, and 2.94 eV for ZnO, ZnO/rGO, and Cu doped-ZnO/rGO, respectively. The decrease in band gap energy with Cu doping may be due to band edge bending caused by doping. With doping, Cu ions provide electrons from its 3d shell which results in the shifting of valence band (O 2p) of ZnO via hybridization of Cu 3d shell, thereby results in a strong Cu 3d-O 2p interaction that narrows the band gap energy [49].

Further, the textural properties of the Cu doped-ZnO/rGO are assessed by nitrogen adsorption-desorption analysis. The nitrogen adsorption-desorption isotherm along with the pore size distribution is presented in Figure 6.4c. The BET isotherm of the sample resembles type IV isotherm representative of the presence of mesopores [50**]**. The specific surface area of the sample is 24.05 m^2g^{-1} with a hysteresis loop of H3 type that is associated with the pore shape of materials consisting of aggregated non-rigid plate-like particles [51]. Using the BJH method in the desorption phase, the average pore diameter

6.2.2 Photocatalytic degradation of methylene blue

The photocatalytic performance of the synthesized Cu-doped ZnO/rGO catalyst is evaluated for the photodegradation of methylene blue (MB) under both UV light and sunlight irradiation. Prior to the photodegradation, the catalyst is added to the MB dye solution and stirred in dark condition for 60 min to attain adsorption-desorption equilibrium. Figure 6.5a and b displays the absorption spectra of MB over Cu-doped ZnO/rGO under UV light and sunlight irradiation respectively. It can be observed that with increasing irradiation time, the absorbance maximum shifts from its initial position which indicates the formation of intermediates upon degradation of the dye [52]. The photodegradation results show that MB is degraded more efficiently under sunlight irradiation compared to that of UV light. This could be due to the reduction of band gap with Cu doping which makes the synthesized photocatalyst visible light responsive. For comparison, bare ZnO and ZnO/rGO are also used to carry out the photodegradation of MB as shown in Figure 6.5c. The photodegradation of MB using Cu-doped ZnO/rGO shows remarkable enhancement compared with pure ZnO and ZnO/rGO. This enhancement in photocatalytic activity of Cu-doped ZnO/rGO photocatalyst could be attributed to the improved light response due to ZnO band gap narrowing with copper

doping. Again, the rGO reduces the recombination rate due to its excellent electrical conductivity and improves the photocatalytic efficiency. Moreover, the high surface area of graphitic materials results in the adsorption of more dye molecules onto the catalyst surface for efficient dye degradation [53].

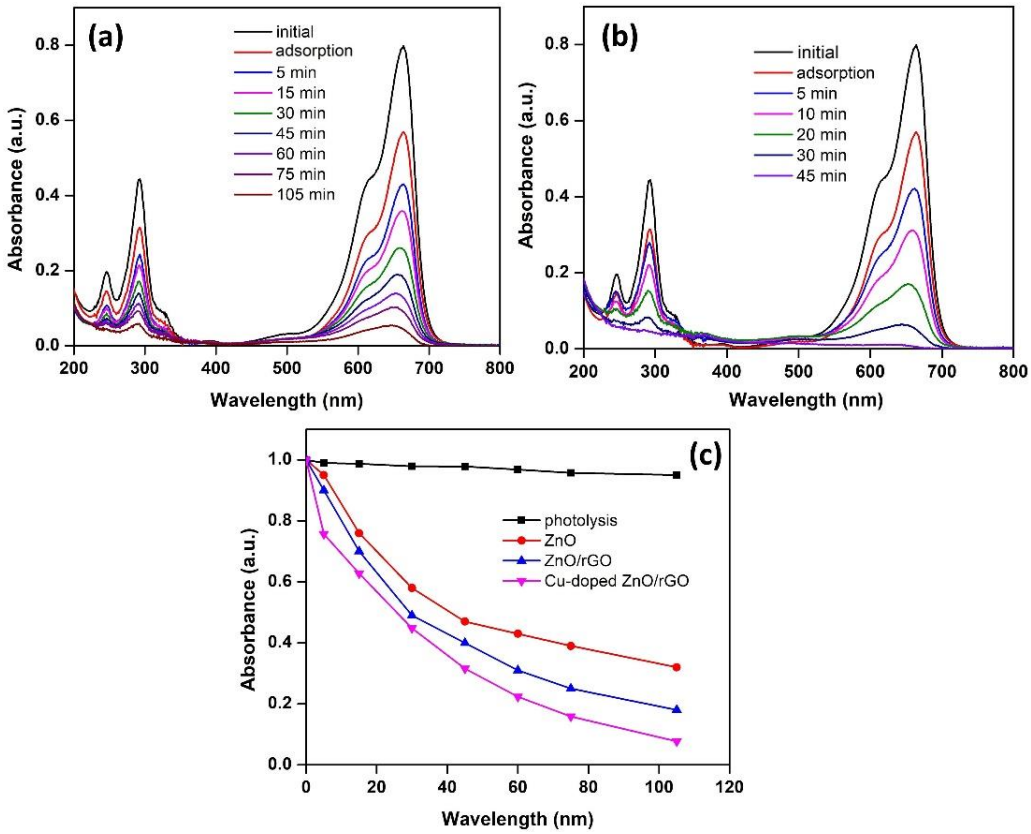

Figure 6.5 UV-visible spectra for photocatalytic degradation of MB over Cu-doped ZnO/rGO under UV light (a) and sunlight (b); Photolysis and photocatalysis of MB over the synthesized photocatalysts (c). Conditions: C_0 = 5 ppm, $V_{solution}$ = 20 mL, catalyst amount = 3 mg, pH = 7.

6.2.2.1 Optimization study

Since the geographical conditions vary with the change in location, the photocatalytic experiments for optimization are further conducted under UV light to have consistency in the results. The effects of various parameters such as catalyst dosage, dye concentration and pH of dye solution on the photocatalytic degradation process are investigated.

6.2.2.1a Effect of catalyst dosage

Figure 6.6a shows the photocatalytic degradation of MB using Cu-doped ZnO/rGO photocatalyst with different amounts of the photocatalyst, viz., 3, 5 and 7 mg, for a fixed dye concentration of 5 ppm. MB degradation gradually increases from 90 to 98% with increasing the catalyst amount from 3 to 5 mg in 105 min. This increase in % degradation is attributable to the increased availability of active catalytic sites upon increasing the catalyst concentration [54]. Upon increasing the catalyst amount to 7 mg, no considerable change in the % degradation as a function of time is observed, which can be substantiated by the fact that the catalyst gets saturated over higher catalyst dose resulting in lower % degradation [55]. Therefore, 5 mg is selected as the optimum amount of catalyst for MB degradation.

6.2.2.1b Effect of dye concentration

The effect of different initial dye concentrations, viz., 5, 10 and 15 ppm on the photocatalytic degradation are tested with a fixed catalyst amount of 5 mg. It is observed from Figure 6.6b that the % degradation decreases upon increasing the initial dye concentration from 5 to 15 ppm. This decrease in % degradation is observed because higher concentration of dye blocks the UV light, resulting in the unavailability of the required number of photons to reach the surface of catalyst for the degradation process [56]. Thus, 5 ppm of dye concentration is chosen as the optimum dye concentration for this study.

6.2.2.1c Effect of pH

The pH of the solution is an important factor that influences the photodegradation efficiency. To find the optimal pH for the photodegradation of MB, the experiments are performed by altering the pH from 2 to 9 and the obtained results are presented in Figure 6.6c. MB is a cationic dye when dissolved in water. At a low pH value (pH = 2), the adsorption of MB on the photocatalyst surface is poor which results in no obvious improvement in % degradation of the dye. This is because, at low pH, i.e., in an acidic medium, positively charged surfaces of the photocatalyst oppose the adsorption of cationic species thereby resulting in lower % degradation [57]. However, with an increase in the pH of the solution from 2 to 9, the % degradation of MB increases. At high pH, i.e., in a basic medium, the surface of the photocatalyst acquires negative

charge and hence it easily assists the degradation of the positively charged MB due to good electrostatic interactions with the photocatalyst.

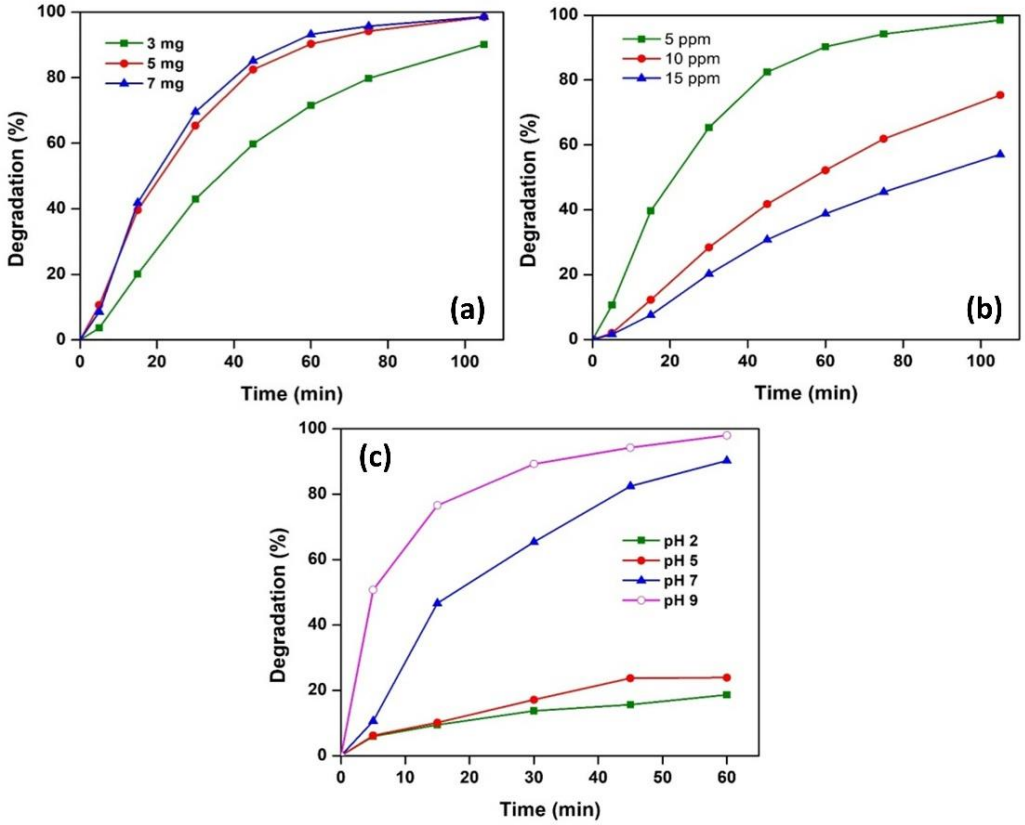

Figure 6.6 Effect of various parameters on the % degradation of MB dye: Catalyst dosage (a), initial dye concentration (b) and pH (c). Conditions: C_0 = 5 ppm, $V_{solution}$ = 20 mL, catalyst dosage = 5 mg, and pH = 7.

6.2.2.2 Kinetic study

The kinetics for photocatalytic degradation of MB over Cu-doped ZnO/rGO is analyzed using 5 ppm of MB dye solution with 5 mg catalyst amount at pH 7. The degradation kinetics follows Langmuir-Hinshelwood first-order kinetics expressed by equation 6.1:

$$\ln\left(\frac{C_0}{C}\right) = K_{app}t \qquad \text{..... (6.1)}$$

where, C_0 and C correspond to concentration of dye at time 0 and t, respectively; and K_{app} is the apparent rate constant in min^{-1}.

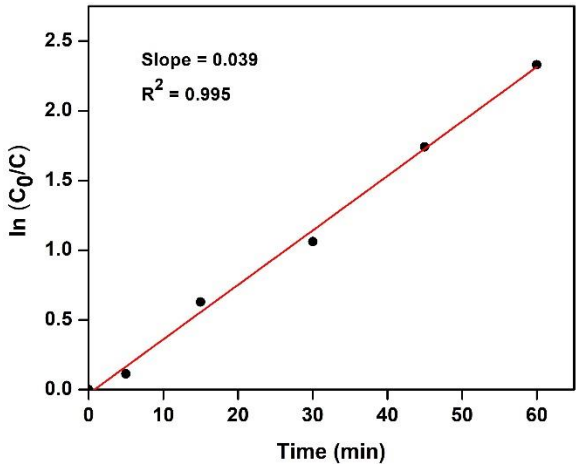

Figure 6.7 Kinetic plot of ln (C_0/C) as a function of time for photocatalytic degradation of MB UV light.

Figure 6.7 shows the variation of $\ln\left(\frac{C_0}{C}\right)$ as a function of time for the photodegradation of MB under UV light. The value of K_{app} is calculated from the slope of the plot of $\ln\left(\frac{C_0}{C}\right)$ versus t and found to be 0.039. The corresponding value of linear regression (R^2) is 0.995 which indicates better fitting of kinetic data to first order model, implying that the photodegradation process of MB over the synthesized Cu-doped ZnO/rGO follows first order kinetics.

6.2.2.3 Proposed mechanism of dye degradation

The enhanced photocatalytic efficiency of the synthesized Cu-doped ZnO/rGO supports the following mechanism for degradation of MB described by equations 6.2–6.8. First, the illumination of the synthesized catalyst with light source having energy greater than the band gap energy results in the generation of electron-hole (e^--h^+) pairs. The presence of rGO with the Cu-doped ZnO forms a heterojunction interface that reduces the e^--h^+ recombination rate and improves the photocatalytic activity of the material. The holes (h^+) react with electron donors (H_2O and OH^-) and form hydroxyl radical ($OH^{\cdot}$) radical. The electrons (e^-) conducted through the rGO sheets react with oxygen (O_2) molecules to produce superoxide radicals ($O_2^{\cdot -}$) and subsequently get converted into $OH^{\cdot}$ radicals via multielectron reduction reactions. Finally, the $OH^{\cdot}$ radicals react with MB dye molecules and decompose them into less toxic products [58].

$$\text{Cu} - \text{doped ZnO/rGO} + \text{hv} \rightarrow h^+ + e^-(\text{rGO}) \quad \ldots\ldots (6.2)$$

$$h^+ + H_2O \rightarrow H^+ + OH^{\cdot} \quad \ldots\ldots (6.3)$$

$$h^+ + OH^- \rightarrow OH^{\cdot} \quad \ldots\ldots (6.4)$$

$$e^-(rGO) + O_2 \rightarrow O_2^{\cdot -} \quad \ldots\ldots (6.5)$$

$$O_2^{\cdot -} + H_2O + H^+ \rightarrow H_2O_2 + OH^- \quad \ldots\ldots (6.6)$$

$$H_2O_2 + e^- \rightarrow OH^{\cdot} + OH^- \quad \ldots\ldots (6.7)$$

$$OH^{\cdot} + MB \rightarrow \text{Degraded Products} \quad \ldots\ldots (6.8)$$

6.2.2.4 Comparative study

Table 6.1 depicts the comparison of photocatalytic activity of Cu-doped ZnO/rGO with various other reported photocatalysts for the degradation of MB. The Cu-doped ZnO/rGO exhibits efficient photocatalytic activity for the degradation of MB under both UV light and sunlight irradiation compared to the other reported catalysts.

Table 6.1 Comparison of photocatalytic activity of Cu-doped ZnO/rGO for MB degradation with reported photocatalysts.

Entry	Catalysts	Light source	Time (min)	Degradation (%)	Ref.
1	Cu_2O	Visible	120	55	59
2	Fe-doped NiO	Visible	60	86	60
3	Ag/Cu_2O	Visible	120	96.5	61
4	Fe-doped In_2O_3	UV	360	83	62
5	Sr-doped ZnO	Visible	80	78.5	63
6	Fe-doped ZnO	UV	180	92	64
7	Mg-doped ZnO	Sunlight	120	96	65
8	Sn-doped ZnO	Sunlight	180	94.5	57
9	Ce-ZnO/graphene	Visible	120	99	54
10	Cu-doped ZnO/rGO	UV	105	98	This work
11	Cu-doped ZnO/rGO	Sunlight	45	99	This work

6.2.2.5 Recyclability test

From an industrial standpoint, the stability and recyclability of a catalyst are two important factors for achieving high efficiency. The reusability of the synthesized Cu-doped ZnO/rGO photocatalyst for the degradation of MB is determined and the results

are shown in Figure 6.8a. The catalyst is separated by centrifugation and washed with water and ethanol and then dried at 80 °C overnight. The regenerated catalyst is then subjected to another cycle of photodegradation under similar experimental conditions keeping MB dye concentration and photocatalyst amount constant at pH 9. It is observed from the figure that the photocatalytic efficiency of the catalyst is retained up to 88 % even after five cycles of reuse. Again, to check the stability of the photocatalyst, XRD analysis of the catalyst is performed after the fifth cycle as shown in figure 6.8b. No obvious change in the XRD pattern is detected substantiating that the crystal structure of the recovered catalyst is retained even after multiple uses thereby confirming the stable nature of the photocatalyst.

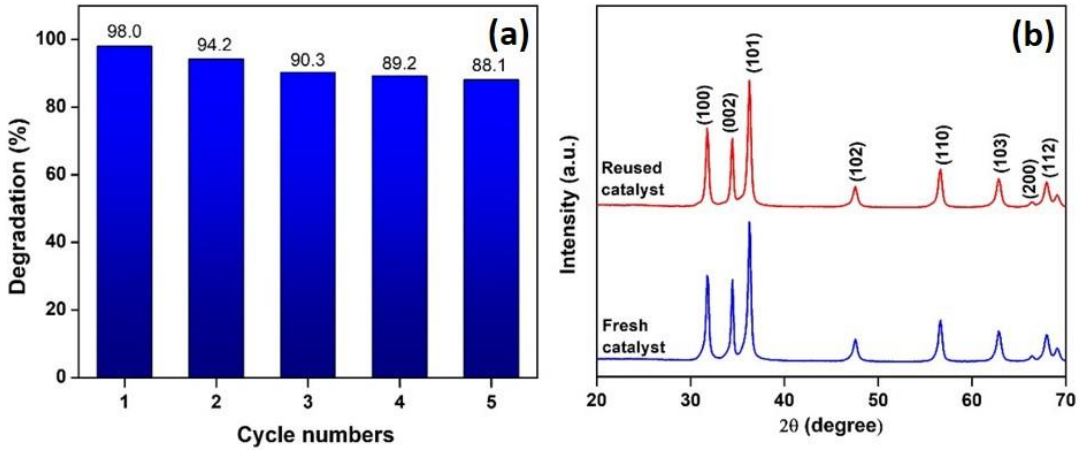

Figure 6.8 Recyclability test for photocatalytic degradation of MB over Cu-doped ZnO/rGO (a), XRD patterns of fresh and reused Cu-doped ZnO/rGO photocatalyst (b). Conditions: C_0 = 5 ppm, $V_{solution}$ = 20 mL, catalyst amount = 5 mg, pH = 9.

In summary, Cu-doped ZnO/rGO synthesized via a simple hydrothermal route has been employed as a photocatalyst for the degradation of MB dye in aqueous solution under UV light and sunlight irradiation. The Cu-doped ZnO/rGO shows excellent activity with ~98% degradation of MB in aqueous solution under UV light. Moreover, the Cu-doped ZnO/rGO photocatalyst exhibits superior activity for MB degradation in comparison to ZnO and ZnO/rGO. This enhanced activity of Cu-doped ZnO/rGO could be attributed to the combined effects of rGO and Cu doping into the ZnO crystal lattice. Again, the effect of various parameters, viz., catalyst dosage, initial dye concentration and pH on the photodegradation process are studied in detail. The kinetic study reveals that the photodegradation process follows first order kinetic model. The recyclability of

the photocatalyst is also studied and found to be active up to five cycles without any significant loss in the photocatalytic activity.

REFERENCES

[1] Islam, T., Repon, M., Islam, T., Sarwar, Z., and Rahman, M. M. Impact of textile dyes on health and ecosystem: A review of structure, causes, and potential solutions. *Environmental Science and Pollution Research*, 1–36, 2022.

[2] Ahmed, J., Thakur, A., and Goyal, A. Industrial wastewater and its toxic effects. In *Biological Treatment of Industrial Wastewater*, pages 1–14, ISBN:978-1-83916-539-9. Royal Society of Chemistry, 2021.

[3] Dhiman, P., Rana, G., Dawi, E. A., Kumar, A., Sharma, G., Kumar, A., and Sharma, J. Tuning the photocatalytic performance of Ni-Zn ferrite catalyst using Nd doping for solar light-driven catalytic degradation of methylene blue. *Water*, 15(1):187, 2023.

[4] Li, S., Lin, Q., Liu, X., Yang, L., Ding, J., Dong, F., Li, Y., Irfan, M., and Zhang, P. Fast photocatalytic degradation of dyes using low-power laser-fabricated Cu_2O–Cu nanocomposites. *RSC Advances*, 8(36):20277–20286, 2018.

[5] Khan, I., Saeed, K., Zekker, I., Zhang, B., Hendi, A. H., Ahmad, A., Ahmad, S., Zada, N., Ahmad, H., Shah, L. A., and Shah, T. Review on methylene blue: Its properties, uses, toxicity and photodegradation. *Water*, 14(2):242, 2022.

[6] Gita, S., Hussan, A., and Choudhury, T. G. Impact of textile dyes waste on aquatic environments and its treatment. *Environment & Ecology*, 35(3C):2349–2353, 2017.

[7] Badawi, A. K., Abd Elkodous, M., and Ali, G. A. Recent advances in dye and metal ion removal using efficient adsorbents and novel nano-based materials: An overview. *RSC Advances*, 11(58):36528–36553, 2021.

[8] Garvasis, J., Prasad, A. R., Shamsheera, K. O., Jaseela, P. K., and Joseph, A. Efficient removal of Congo red from aqueous solutions using phytogenic aluminum sulfate nano coagulant. *Materials Chemistry and Physics*, 251:123040, 2020.

[9] Moradihamedani, P. Recent advances in dye removal from wastewater by membrane technology: A review. *Polymer Bulletin*, 79(4):2603–2631, 2022.

[10] Rafiq, A., Ikram, M., Ali, S., Niaz, F., Khan, M., Khan, Q., and Maqbool, M. Photocatalytic degradation of dyes using semiconductor photocatalysts to clean industrial water pollution. *Journal of Industrial and Engineering Chemistry*, 97:111–128, 2021.

[11] Khan, M. S. J., Kamal, T., Ali, F., Asiri, A. M., and Khan, S. B. Chitosan-coated polyurethane sponge supported metal nanoparticles for catalytic reduction of organic pollutants. *International Journal of Biological Macromolecules*, 132:772–783, 2019.

[12] Javaid, R. and Qazi, U. Y. Catalytic oxidation process for the degradation of synthetic dyes: An overview. *International Journal of Environmental Research and Public Health*, 16(11):2066, 2019.

[13] Rafiq, A., Ikram, M., Ali, S., Niaz, F., Khan, M., Khan, Q., and Maqbool, M. Photocatalytic degradation of dyes using semiconductor photocatalysts to clean industrial water pollution. *Journal of Industrial and Engineering Chemistry*, 97:111–128, 2021.

[14] Yang, Y., Xiong, Z., Wang, Z., Liu, Y., He, Z., Cao, A., Zhou, L., Zhu, L., and Zhao, S. Super-adsorptive and photo-regenerable carbon nanotube based membrane for highly efficient water purification. *Journal of Membrane Science*, 621:119000, 2021.

[15] Su, F., Li, P., Huang, J., Gu, M., Liu, Z., and Xu, Y. Photocatalytic degradation of organic dye and tetracycline by ternary Ag_2O/AgBr–CeO_2 photocatalyst under visible-light irradiation. *Scientific Reports*, 11(1):1–13, 2021.

[16] Kadam, A. N., Kim, T. G., Shin, D. S., Garadkar, K. M., and Park, J. Morphological evolution of Cu doped ZnO for enhancement of photocatalytic activity. *Journal of Alloys and Compounds*, 710:102–113, 2017.

[17] Zare, E. N., Iftekhar, S., Park, Y., Joseph, J., Srivastava, V., Khan, M. A., Makvandi, P., Sillanpaa, M., and Varma, R. S. An overview on non-spherical semiconductors for heterogeneous photocatalytic degradation of organic water contaminants. *Chemosphere*, 280:130907, 2021.

[18] Akbari, A., Sabouri, Z., Hosseini, H. A., Hashemzadeh, A., Khatami, M., and Darroudi, M. Effect of nickel oxide nanoparticles as a photocatalyst in dyes degradation and evaluation of effective parameters in their removal from aqueous environments. *Inorganic Chemistry Communications*, 115:107867, 2020.

[19] Balcha, A., Yadav, O. P., and Dey, T. Photocatalytic degradation of methylene blue dye by zinc oxide nanoparticles obtained from precipitation and sol-gel methods. *Environmental Science and Pollution Research*, 23(24):25485–25493, 2016.

[20] Darroudi, M., Bratovcic, A., Sabouri, Z., and Moghaddas, S. S. T. H. Removal of organic dyes from wastewaters using metal oxide nanoparticles. In *Sustainable Management of Environmental Contaminants*, pages 483–508. Springer, Cham., 2022.

[21] Weldegebrieal, G. K. Synthesis method, antibacterial and photocatalytic activity of ZnO nanoparticles for azo dyes in wastewater treatment: A review. *Inorganic Chemistry Communications*, 120:108140, 2020.

[22] Kharroubi, B., Bousmaha, M., Bezzerrouk, M. A., Akriche, A., Naceur, R., Bensassi, K. B., Zahafi, K., Zoukel, A., Abdelkrim, M., Bedrouni, M., and Bouslama, M. H. Photocatalytic efficiency of undoped and Cu-doped ZnO thin films coated inside transparent glass tube as one-piece photoreactor. *Applied Surface Science*, 601:154121, 2022.

[23] Vinitha, V., Preeyanghaa, M., Vinesh, V., Dhanalakshmi, R., Neppolian, B., and Sivamurugan, V. Two is better than one: Catalytic, sensing and optical applications of doped zinc oxide nanostructures. *Emergent Materials*, 4(5):1093–1124, 2021.

[24] Shah, A. A., Bhatti, M. A., Tahira, A., Chandio, A. D., Channa, I. A., Sahito, A. G., Chalangar, E., Willander, M., Nur, O., and Ibupoto, Z. H. Facile synthesis of copper doped ZnO nanorods for the efficient photo degradation of methylene blue and methyl orange. *Ceramics International*, 46(8):9997–10005, 2020.

[25] Esgin, H., Caglar, Y., and Caglar, M. Photovoltaic performance and physical characterization of Cu doped ZnO nanopowders as photoanode for DSSC. *Journal of Alloys and Compounds*, 890:161848, 2022.

[26] Khalid, A., Ahmad, P., Khan, A., Muhammad, S., Khandaker, M. U., Alam, M., Asim, M., Din, I. U., Chaudhary, R. G., Kumar, D., and Sharma, R. Effect of Cu doping on ZnO nanoparticles as a photocatalyst for the removal of organic wastewater. *Bioinorganic Chemistry and Applications*, 2022:9459886, 2022.

[27] Seo, Y. S. and Oh, S. G. Controlling the recombination of electron-hole pairs by changing the shape of ZnO nanorods via sol-gel method using water and their enhanced photocatalytic properties. *Korean Journal of Chemical Engineering*, 36(12):2118–2124, 2019.

[28] Jiang, H., Zhang, X., Gu, W., Feng, X., Zhang, L., and Weng, Y. Synthesis of ZnO particles with multi-layer and biomorphic porous microstructures and

ZnO/rGO composites and their applications for photocatalysis. *Chemical Physics Letters*, 711:100–106, 2018.

[29] Mohammad, A., Ahmad, K., Qureshi, A., Tauqeer, M., and Mobin, S. M. Zinc oxide-graphitic carbon nitride nanohybrid as an efficient electrochemical sensor and photocatalyst. *Sensors and Actuators B: Chemical*, 277:467–476, 2018.

[30] Sampaio, M. J., Bacsa, R. R., Benyounes, A., Axet, R., Serp, P., Silva, C. G., Silva, A. M., and Faria, J. L. Synergistic effect between carbon nanomaterials and ZnO for photocatalytic water decontamination. *Journal of Catalysis*, 331:172–180, 2015.

[31] Kumar, P., Som, S., Pandey, M. K., Das, S., Chanda, A., and Singh, J. Investigations on optical properties of ZnO decorated graphene oxide (ZnO@ GO) and reduced graphene oxide (ZnO@ r-GO). *Journal of Alloys and Compounds*, 744:64–74, 2018.

[32] Shkir, M., Palanivel, B., Khan, A., Kumar, M., Chang, J. H., Mani, A., and AlFaify, S. Enhanced photocatalytic activities of facile auto-combustion synthesized ZnO nanoparticles for wastewater treatment: An impact of Ni doping. *Chemosphere*, 291:132687, 2022.

[33] Alkallas, H., Ben Gouider Trabelsi, A., Nasser, R., Fernandez, S., Song, J. M., and Elhouichet, H. Promising Cr-doped ZnO nanorods for photocatalytic degradation facing pollution. *Applied Sciences*, 12(1):34, 2022.

[34] Khalid, N. R., Ishtiaq, H., Ali, F., Tahir, M. B., Naeem, S., Ul-Hamid, A., Ikram, M., Iqbal, T., Kamal, M. R., Alrobei, H., and Alzaid, M. Synergistic effects of Bi and N doped on ZnO nanorods for efficient photocatalysis. *Materials Chemistry and Physics*, 289:126423, 2022.

[35] Yousefi, R., Beheshtian, J., Seyed–Talebi, S. M., Azimi, H. R., and Jamali–Sheini, F. Experimental and theoretical study of enhanced photocatalytic activity of Mg-doped ZnO NPs and ZnO/rGO nanocomposites. *Chemistry–An Asian Journal*, 13(2):194–203, 2018.

[36] Hanh, N. T., Tri, N. L. M., Van Thuan, D., Tung, M. H. T., Pham, T. D., Minh, T. D., Trang, H. T., Binh, M. T., and Nguyen, M. V. Monocrotophos pesticide effectively removed by novel visible light driven Cu doped ZnO photocatalyst. *Journal of Photochemistry and Photobiology A: Chemistry*, 382:111923, 2019.

[37] Singhal, N., Selvaraj, S., Sivalingam, Y., and Venugopal, G. Study of photocatalytic degradation efficiency of rGO/ZnO nano-photocatalyst and their performance analysis using scanning Kelvin probe. *Journal of Environmental Chemical Engineering*, 10(2):107293, 2022.

[38] Gollu, S. R., Sharma, R., Srinivas, G., Kundu, S., and Gupta, D. Incorporation of silver and gold nanostructures for performance improvement in P3HT: PCBM inverted solar cell with rGO/ZnO nanocomposite as an electron transport layer. *Organic Electronics*, 29:79–87, 2016.

[39] Bhaumik, A. and Narayan, J. Wafer scale integration of reduced graphene oxide by novel laser processing at room temperature in air. *Journal of Applied Physics*, 120(10):105304, 2016.

[40] Tan, S. M., Ambrosi, A., Chua, C. K., and Pumera, M. Electron transfer properties of chemically reduced graphene materials with different oxygen contents. *Journal of Materials Chemistry A*, 2(27):10668–10675, 2014.

[41] Al-Gaashani, R., Radiman, S., Daud, A. R., Tabet, N., and Al-Douri, Y. J. C. I. XPS and optical studies of different morphologies of ZnO nanostructures prepared by microwave methods. *Ceramics International*, 39(3):2283–2292, 2013.

[42] Rooydell, R., Brahma, S., Wang, R. C., Modaberi, M. R., Ebrahimzadeh, F., and Liu, C. P. Cu doped ZnO nanorods with controllable Cu content by using single metal organic precursors and their photocatalytic and luminescence properties. *Journal of Alloys and Compounds*, 691:936–945, 2017.

[43] Qu, G., Fan, G., Zhou, M., Rong, X., Li, T., Zhang, R., Sun, J., and Chen, D. Graphene-modified ZnO nanostructures for low-temperature NO_2 sensing. *ACS Omega*, 4(2):4221–4232, 2019.

[44] Zhang, Q., Gai, L., Cai, K., and Wang, E. Synergistic effect of In doped ZnO/rGO anode material for rechargeable Zn–Ni secondary battery with high specific capacity. *ChemistrySelect*, 5(34):10643–10647, 2020.

[45] Rodwihok, C., Wongratanaphisan, D., Thi Ngo, Y. L., Khandelwal, M., Hur, S. H., and Chung, J. S. Effect of GO additive in ZnO/rGO nanocomposites with enhanced photosensitivity and photocatalytic activity. *Nanomaterials*, 9(10):1441, 2019.

[46] Salim, M. A., Khattak, G. D., Tabet, N., and Wenger, L. E. X-Ray photoelectron spectroscopy (XPS) studies of copper–sodium tellurite glasses. *Journal of Electron Spectroscopy and Related Phenomena*, 128(1):75–83, 2003.

[47] Van Tuan, P., Phuong, T. T., Tan, V. T., Nguyen, S. X., and Khiem, T. N. *In-situ* hydrothermal fabrication and photocatalytic behavior of ZnO/reduced graphene oxide nanocomposites with varying graphene oxide concentrations. *Materials Science in Semiconductor Processing*, 115:105114, 2020.

[48] Zak, A. K., Abrishami, M. E., Majid, W. A., Yousefi, R., and Hosseini, S. M. Effects of annealing temperature on some structural and optical properties of ZnO nanoparticles prepared by a modified sol–gel combustion method. *Ceramics International*, 37(1):393–398, 2011

[49] Ahn, K. S., Deutsch, T., Yan, Y., Jiang, C. S., Perkins, C. L., Turner, J., and Al-Jassim, M. Synthesis of band-gap-reduced p-type ZnO films by Cu incorporation. *Journal of Applied Physics*, 102(2):023517, 2007.

[50] Tian, H., Luo, J., Zhang, K., Ma, C., Qi, Y., Zhan, S., Liu, X., Li, M., and Liu, H. Synergistic photocatalytic-adsorption removal of basic magenta effect of AgZnO/polyoxometalates nanocomposites. *Nanoscale Research Letters*, 16(1):1–12, 2021.

[51] Bardestani, R.; Patience, G. S.; Kaliaguine, S. Experimental methods in chemical engineering: Specific surface area and pore size distribution measurements-BET, BJH, and DFT. *The Canadian Journal of Chemical Engineering*, 97(11):2781−2791, 2019.

[52] Beura, R. and Thangadurai, P. Effect of Sn doping in ZnO on the photocatalytic activity of ZnO-graphene nanocomposite with improved activity. *Journal of Environmental Chemical Engineering*, 6(4):5087–5100, 2018.

[53] Bradder, P., Ling, S. K., Wang, S., and Liu, S. Dye adsorption on layered graphite oxide. *Journal of Chemical & Engineering Data*, 56(1):138–141, 2011.

[54] Zhang, S., Fan, Q., Gao, H., Huang, Y., Liu, X., Li, J., Xu, X., and Wang, X. Formation of Fe_3O_4@MnO_2 ball-in-ball hollow spheres as a high performance catalyst with enhanced catalytic performances. *Journal of Materials Chemistry A*, 4(4):1414–1422, 2016.

[55] Jawed, A., Verma, R., Saxena, V., and Pandey, L. M. Photocatalytic metal nanoparticles: A green approach for degradation of dyes. In Shah, M., Dave, S.,

and Das, J., editors, *Photocatalytic Degradation of Dyes*, pages 251–275. Elsevier, 2021.

[56] Rauf, M. A., Meetani, M. A., and Hisaindee, S. An overview on the photocatalytic degradation of azo dyes in the presence of TiO_2 doped with selective transition metals. *Desalination*, 276(1–3):13–27, 2011.

[57] Ikram, M., Abid, N., Haider, A., Ul-Hamid, A., Haider, J., Shahzadi, A., Nabgan, W., Goumri-Said, S., Butt, A. R., and Kanoun, M. B. Toward efficient dye degradation and the bactericidal behavior of Mo-doped La_2O_3 nanostructures. *Nanoscale Advances*, 4(3):926–942, 2022.

[58] Adam, R. E., Alnoor, H., Pozina, G., Liu, X., Willander, M., and Nur, O. Synthesis of Mg-doped ZnO NPs via a chemical low-temperature method and investigation of the efficient photocatalytic activity for the degradation of dyes under solar light. *Solid State Sciences*, 99:106053, 2020.

[59] Kumar, S., Parlett, C. M., Isaacs, M. A., Jowett, D. V., Douthwaite, R. E., Cockett, M. C., and Lee, A. F. Facile synthesis of hierarchical Cu_2O nanocubes as visible light photocatalysts. *Applied Catalysis B: Environmental*, 189:226–232, 2016.

[60] Khatri A. and P. S. Rana. Visible light assisted photocatalysis of methylene blue and rose bengal dyes by iron doped NiO nanoparticles prepared via chemical co-precipitation. *Physica B:Condensed Matter*, 579:411905, 2020.

[61] Sun, Y., Cai, L., Liu, X., Cui, Z., and Rao, P. Tailoring heterostructures of Ag/Cu_2O hybrids for enhanced photocatalytic degradation. *Journal of Physics and Chemistry of Solids*, 111:75–81, 2017.

[62] Jabeen, S., Iqbal, J., Arshad, A., Awan, M. S., and Warsi, M. F. $(In_{1-x}Fe_x)_2O_3$ nanostructures for photocatalytic degradation of various dyes. *Materials Chemistry and Physics*, 243:122516, 2020.

[63] Yousefi, R., Farid, J.-S., Cheraghizade, M., Sara, K.-G., Sáaedi, A., Huang, N. M., Basirun, W. J., and Azarang, M. Enhanced visible-light photocatalytic activity of strontium-doped zinc oxide nanoparticles. *Materials Science in Semiconductor Processing*, 32:152–159, 2015.

[64] Isai, K. A. and Shrivastava, V. S. Photocatalytic degradation of methylene blue using ZnO and 2% Fe–ZnO semiconductor nanomaterials synthesized by sol–gel method: A comparative study. *SN Applied Sciences*, 1(10):1–11, 2019.

[65] Adam, R. E., Alnoor, H., Pozina, G., Liu, X., Willander, M., and Nur, O. Synthesis of Mg-doped ZnO NPs via a chemical low-temperature method and investigation of the efficient photocatalytic activity for the degradation of dyes under solar light. *Solid State Sciences*, 99:106053, 2020.